

Article

Research on the Hydrodynamic Performance of a Pentamaran in Calm Water and Regular Waves

Bowen Zhao ^{1,2,3} , Haoyu Jiang ^{1,*}, Jiyuan Sun ² and Dapeng Zhang ³ ¹ School of Electronics and Information Engineering, Guangdong Ocean University, Zhanjiang 524088, China² Ocean College, Zhejiang University, Zhoushan 316021, China³ Ship and Maritime College, Guangdong Ocean University, Zhanjiang 524088, China

* Correspondence: jianghy@gdou.edu.cn

Abstract: As a typical multi-hull ship, the pentamaran has a wider deck, higher damage stability, and low-speed seaworthiness in harsh sea conditions compared with other multi-hull types such as the catamaran and trimaran, having more potential for becoming a new type of freight merchant ship in line with the development trend of the marine economy. In this paper, on the basis of the finite volume method, the numerical simulations and detailed comparative analysis of the monohull and pentamaran in viscous flow were carried out. The resistance prediction in calm water and regular waves and the changes of each resistance component of the pentamaran were explored. The dynamic fluid body interaction (DFBI) module was used for the calculations in calm water, and the overset mesh was used for the calculations in regular waves. The results show that in calm water, the adverse effect of the side hulls on the resistance was mainly reflected in the low-speed range. In the high-speed range, the influence of the side hulls on the resistance can be ignored. At high speeds, the main hull and side hulls of the pentamaran will produce favorable wave-making interference, thereby improving the wave-making performance of the pentamaran. In regular waves, although the added resistance of the pentamaran increased most of the time, its amplitude was smaller than that of the monohull under the same wave condition. This work provides a technical basis for the research on the design and hydrodynamic performance of the pentamaran.

Keywords: pentamaran; monohull; RANS; regular waves; hydrodynamic performance



Citation: Zhao, B.; Jiang, H.; Sun, J.; Zhang, D. Research on the Hydrodynamic Performance of a Pentamaran in Calm Water and Regular Waves. *Appl. Sci.* **2023**, *13*, 4461. <https://doi.org/10.3390/app13074461>

Academic Editor: Francesca Scargiali

Received: 3 March 2023

Revised: 20 March 2023

Accepted: 28 March 2023

Published: 31 March 2023



Copyright: © 2023 by the authors. Licensee MDPI, Basel, Switzerland. This article is an open access article distributed under the terms and conditions of the Creative Commons Attribution (CC BY) license (<https://creativecommons.org/licenses/by/4.0/>).

1. Introduction

Global climate change may be one of the most challenging environmental problems facing society [1,2]. Freight merchant ships and containerships are among the largest maritime emitters of CO₂. The scarcity of fossil fuels and rising concern about global warming have prompted international organizations to improve vessel efficiency and push the development of ship energy technologies such as wing systems, propeller boss cap fins, reaction rudders, and high-performance ships [3,4].

The pentamaran is a new type of high-performance ship developed at the end of the 20th century. Its structure consists of a slender main hull and four side hulls distributed on both sides of the main hull. Due to its advantages of low high-speed resistance, good stability, and high seaworthiness, the pentamaran has good application prospects in both commercial and military ships [5]. It is believed that a pentamaran can carry more cargo compared to traditional commercial containerships, thereby increasing cargo volume and reducing polluting gas emissions. At the same time, the speed range of the pentamaran varies widely and is also suitable for speed variations from low to high. This also has a positive effect on environmental protection [6].

Since it was proposed, many scholars have studied the hydrodynamic performance of the pentamaran. Nigel et al. [7] and Duson [8,9] completed the preliminary design of a transatlantic pentamaran container ship with a loading weight of up to 8000 tons and a

service speed of 40 knots, carrying out model tests and optimization of the pentamaran. The pentamaran designed by Nigel et al. is shown in Figure 1. This was a relatively early pentamaran design proposal. Most subsequent studies were conducted on the basis of this design. Wu and Moan [10] conducted nonlinear time-domain simulations of ship motion and load effects on a same pentamaran container ship under different sea conditions. The results showed that when the ship's hull was treated as a rigid body, the predicted wave-induced design vertical sagging and hogging bending moments amidships were comparable to the rule values. The structural dynamic effects, mainly whipping, would increase the design values by 30% to 50% in the numerical prediction. He et al. [11] explored the resistance characteristics of the pentamaran using experiments and studied the influence of parameters of rear side hulls including the shape line, position, and displacement on the resistance characteristics. The results showed that the rear side hulls should use a conventional molded line. Duan [12,13] and Chen [14] studied the hydrodynamic performance of the pentamaran in calm water. Through the research, it was shown that the computational fluid dynamics (CFD) method could be used to calculate and simulate the hydrodynamic characteristics of the multi-hull ship with free surface. Combined with the classical linearized free surface conditions, Tarafder [15] proposed a boundary element method based on the potential flow theory to predict the hydrodynamic performance of a pentamaran in unbounded water at a constant speed. He came to the conclusion that when Froude number F_n was greater than 0.8, the wave-making interference between the main hull and side hulls was small, which could significantly reduce the wave-making resistance. Waskito et al. [16–18] studied the resistance characteristics of the pentamaran with variable side hull spacing and position using the towing tests, finding that the influence of the side body position on the resistance was closely related to F_n . In recent years, Yanuar and his team have been active in the research of the pentamaran, covering the overall arrangement of side hulls [19], the installation layout of symmetrical and asymmetrical side bodies [20,21], drag reduction of X-shaped pentamarans [22], and the optimization of main and side hulls profiles [23,24]. Cui et al. [25] investigated the resistance performance of a pentamaran with different outrigger inclination angles. The results showed that the influence of the front outrigger inclination angle change on the resistance of the pentamaran had a certain rule, and the resistance of the pentamaran could be reduced by adjusting the front outrigger inclination angle.



Figure 1. The concept design of a pentamaran [7].

Most of the above research was carried out via experiments, and some of them were carried out through numerical simulations. The biggest advantage of experimental research is to provide reliable data for subsequent research to replicate. Ship model tests are commonly used to analyze the hydrodynamic performance of ships. The accuracy of ship model tests has also been widely recognized by the engineering community. However, the disadvantages of ship model tests are also obvious: time-consuming nature and high economic costs. The data that can be measured each time are very limited, and during the test process, uncertain factors such as scale effects and test equipment accuracy can bring many test errors that need to be corrected. CFD is a numerical simulation method that

considers the effect of fluid viscosity [26–29]. With the continuous improvement of CFD, the application of CFD in ship hydrodynamics is becoming increasingly more common [30–37]. Akbarzadeh et al. [38], for example, used the finite volume method to numerically simulate the flow field around a Series60 ship in the range of medium and low speeds. Yang et al. [39] studied the additional resistance of three different bows of KVLCC2 in short waves using CFD. Cheng et al. [40] combined the optimization algorithm and CFD to optimize the bow of a 1300TEU container ship and realized the optimal design of drag reduction for this ship type. Ali et al. [41] used the open source CFD software OpenFOAM to numerically predict the hydrostatic resistance of two fishing boats. Cheol-Min Lee et al. [42] used a 66KDWT bulk carrier as the parent ship and calculated the resistance characteristics of the pointed bow and the blunt bow in calm water and waves using CFD. Larsson et al. [43] predicted the wave induced force of irregular waves on slender ships on the basis of CFD and found that the CFD results were in good agreement with the experimental fluid dynamics (EFD) results through comparison. Carrica et al. [44] used the CFD method to directly simulate the zigzag maneuver of KCS in shallow water, finding that they can better predict the parameters such as force and torque. According to the literature, on the basis of viscous flow theory, the CFD method has the advantages of short cycle and low cost, which cannot be replaced by ship model experiments. The simulation results can also achieve high calculation accuracy.

This paper aims at investigating the hydrodynamic performance of the pentamaran in calm water and regular waves. According to the literature, the hydrodynamic performance of the pentamaran has been discussed and verified. However, most of the research on the performance of the pentamaran was conducted in calm water. There are few reports on hydrodynamic performance of the pentamaran in waves. In most cases, ships do not sail in calm water, but in waves. Therefore, the study of the hydrodynamic performance of a pentamaran in waves is helpful for its hydrodynamic design, thereby playing a positive role in the shipping industry and in environmental protection. On the basis of the CFD method, the dynamic fluid body interaction module and the overset mesh were used to simulate the motion response of the pentamaran. The simulation results were also compared with those of the monohull in order to explore the changes in the resistance components and reveal the drag reduction mechanism of the pentamaran during high-speed sailing.

2. Geometry and Simulation Conditions

2.1. Geometry of the Model

The pentamaran used in this paper is based on a shuttle SV-O monohull with a simple modification of the shape line to accommodate the installation of the front and rear side hulls of the pentamaran. An X-shaped symmetrical shape was selected, and the Wigley hull was used as the front and rear side hulls [11]. The main particulars and the geometry of the full-scale monohull are shown in Table 1 and Figure 2, respectively.

Table 1. Main particulars of the monohull.

Particulars	Symbols/Unit	Value
Overall length	L_{OA}/m	22.022
Length at the water line	L_{wl}/m	21.484
Breadth	B_{wl}/m	3.742
Molded depth	D/m	1.927
Draft	d/m	1.000
Displacement	∇/m^3	26.877
Wetter area	S/m^2	72.250
Waterline coefficient	C_w	0.687
Block coefficient	C_b	0.342



Figure 2. The geometry of the monohull.

The main hull of the pentamaran is the same as the monohull. The design of the front and rear hulls usually meets three conditions: first, the length of the rear hull generally does not exceed 1/3 of the waterline length of the main hull; second, the displacement of the rear hull is controlled within 15% of the total displacement; third, the front hull is usually higher in the horizontal position than the rear hull and can be lifted out of the water surface when sailing at high speed. On the basis of the above conditions, this paper designed a side hull shape line with a thinner front than the rear (shown in Figure 3). The main particulars of the front hull and the rear hull are shown in Tables 2 and 3, respectively.



Figure 3. The geometry of the pentamaran.

Table 2. Main particulars of the front hull.

Particulars	Symbols/Unit	Value
Overall length	L_1/m	4.899
Breadth	B_1/m	0.686
Draft	d_1/m	0.543
Displacement	∇_1/m^3	1.325
Wetter area	S_1/m^2	7.420

Table 3. Main particulars of the rear hull.

Particulars	Symbols/Unit	Value
Overall length	L_1/m	5.270
Breadth	B_1/m	0.672
Draft	d_1/m	0.965
Displacement	∇_1/m^3	2.015
Wetter area	S_1/m^2	11.07

2.2. Simulation Conditions

In order to comprehensively analyze and compare the hydrodynamic performance of the pentamaran and the monohull, there are five speeds in calm water, two low speeds, one medium speed, and two high speeds. The choice of speeds is based on the Froude number F_n [25]. When a ship is sailing, motions such as pitch, heave, roll, sway, and yaw occur. It is generally believed that the pitch and heave motions are the main reasons for the increase in ship resistance. Therefore, in order to simplify the calculation, only the two degrees of freedom, pitch and heave, are released. The simulation conditions in calm water are shown in Table 4.

Table 4. Simulation conditions in calm water.

Case	Speed/kn	Speed/(m/s)	F_n	Degree of Freedom
1	5	2.572	0.175	Pitch and heave
2	10	5.144	0.351	Pitch and heave
3	15	7.716	0.527	Pitch and heave
4	20	10.288	0.703	Pitch and heave
5	25	12.860	0.879	Pitch and heave

The inlet flow velocity is set according to the Froude number F_n based on hull length, where the F_n is defined as follows:

$$F_n = \frac{V}{\sqrt{gL}} \quad (1)$$

In the wave simulation, the speed is fixed at $F_n = 0.527$ and two head wave environments are selected with different wave periods. The simulation conditions in waves are shown in Table 5. At the initial moment of calculation, the hull remains upright, and the degree of freedom of the hull is released after 0.5 s. The calculation time is 20 s.

Table 5. Simulation conditions in calm water.

Case	Speed/kn	Wave Height/m	Wave Period/s	Degree of Freedom
6	10.288	1	π	Pitch and heave
7	10.288	1	$\pi/2$	Pitch and heave

3. Mathematical Formulation

3.1. Governing Equation

The RANS equation was used for the numerical simulations. For the three-dimensional incompressible flows, the continuity and momentum equations are written as follows:

$$\frac{\partial (\rho \bar{u}_i)}{\partial x} = 0 \quad (2)$$

$$\rho \frac{\partial \bar{u}_i}{\partial t} + \rho \bar{u}_j \frac{\partial \bar{u}_i}{\partial x_j} = \rho \bar{f}_i - \frac{\partial \bar{p}}{\partial x_i} + \frac{\partial}{\partial x_j} (\mu \frac{\partial \bar{u}_i}{\partial x_j} - \rho \overline{u'_i u'_j}) \quad (3)$$

where \bar{p} is the mean pressure, and ρ and μ define the density and dynamic viscosity of fluid, respectively. \bar{u}_i is the averaged velocity vector and $\overline{u'_i u'_j}$ denotes the Reynolds stresses.

The CFD simulations were carried out in the commercial software STAR-CCM+. The finite volume method (FVM) was used to discretize the RANS equations. The Realizable k- ϵ model was applied as the turbulence model. The convective terms were discretized using a second-order upwind scheme, the diffusion terms were discretized by a central differences scheme, and the temporal terms were discretized by adopting a second-order backward Euler scheme. The Semi-Implicit Method for Pressure-Linked Equations (SIMPLE) algorithm was applied to deal with pressure–velocity coupling. The volume of fluid (VOF) method was used to capture the evolution of free surface for the two-phase flow. The all-Y+ treatment was employed for near wall modeling, which applies wall function for coarse meshes and resolves viscous sub-layer for fine meshes. The dynamic fluid body interaction (DFBI) module combined with overset mesh was applied to consider ship motions in pitch and heave degree of freedom.

3.2. Overset Mesh

Overset mesh is composed of a series of finite mesh volume grids, which overlap each other to form a single computational domain. In overset mesh, grid cells are grouped into active, inactive, or receptor grid cells. In the active grid element, the discrete control equations are solved. In inactive grid cells, no equations are solved, but if the overset mesh

area is moving, these grid cells can become active. The main advantage of this method is that it can deal with complex geometric structures and relative motion of objects in dynamic simulation. Generally, the computational domain consists of a background grid and one or more small overlapping grid regions [45,46]. The overset mesh is an efficient form of dealing with complex shape mesh layouts and is widely used due to its convenience of mesh generation. It is very convenient to use dynamic overset mesh for complex structures with relative motion. The relative motion between sub-domains does not require mesh deformation, nor does it need to regenerate the mesh. It is only necessary to define its motion law in the sub-domains. The schematic diagram of the overset mesh is shown in Figure 4, where C represents the node center of overset area and N represents the node center of the surrounding mesh used for data exchange.

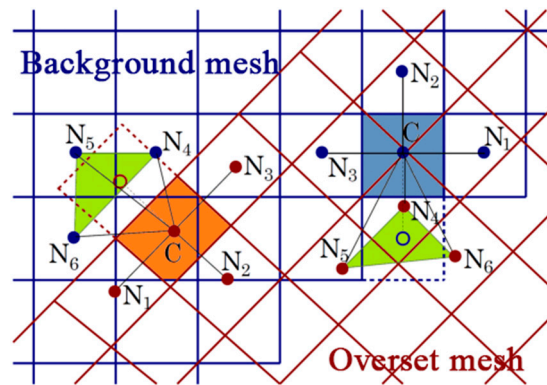


Figure 4. The schematic diagram of the overset mesh.

3.3. Wave-Generating Method

For wave generation, a fifth-order wave was modeled with a fifth-order approximation to the Stokes theory of waves with the given wave height and wave period. The relevant equations of the Stokes fifth-order wave are as follows:

Velocity potential function:

$$\Phi = \frac{c}{k} \sum_{n=1}^5 \lambda_n \cosh nk(z + d) \sin n(kx - \omega t) \tag{4}$$

Wave surface equation:

$$\eta = \frac{1}{k} \sum_{n=1}^5 \lambda_n \cos n(kx - \omega t) \tag{5}$$

The velocity of the water mass point in the horizontal and vertical directions:

$$u_x = \frac{\partial \Phi}{\partial x} = c \sum_{n=1}^5 n \lambda_n \cosh nk(z + d) \cos n(kx - \omega t) \tag{6}$$

$$u_z = \frac{\partial \Phi}{\partial z} = c \sum_{n=1}^5 n \lambda_n \sinh nk(z + d) \sin n(kx - \omega t) \tag{7}$$

The acceleration of the water mass point in the horizontal and vertical directions:

$$a_x = \frac{\partial u_x}{\partial t} = \omega c \sum_{n=1}^5 n^2 \lambda_n \cosh nk(z + d) \cos n(kx - \omega t) \tag{8}$$

$$a_z = \frac{\partial u_z}{\partial t} = -\omega c \sum_{n=1}^5 n^2 \lambda_n \sinh nk(z + d) \sin n(kx - \omega t) \tag{9}$$

where c refers to the wave velocity, k refers to the wave number, ω refers to the angular frequency, d refers to the water depth, and λ is a constant for each wave.

To avoid the reflection from the exit boundary, a damping method was used for the wave generation [47]. The expression of the momentum equation after damping modification is defined as

$$\frac{\partial u}{\partial t} + u \frac{\partial u}{\partial x} + v \frac{\partial u}{\partial y} = g_x - \frac{1}{\rho} \frac{\partial p}{\partial x} + \nu \left[\frac{\partial^2 u}{\partial x^2} + \frac{\partial^2 u}{\partial y^2} \right] - \mu(x)u \tag{10}$$

$$\frac{\partial v}{\partial t} + u \frac{\partial v}{\partial x} + v \frac{\partial v}{\partial y} = g_y - \frac{1}{\rho} \frac{\partial p}{\partial y} + \nu \left[\frac{\partial^2 v}{\partial x^2} + \frac{\partial^2 v}{\partial y^2} \right] - \mu(x)v \tag{11}$$

where $\mu(x)$ is the damping coefficient varying with the x -position as follows:

$$\mu(x) = \begin{cases} a_s(x - x_0)/L_s & x > x_0 \\ 0 & x \leq x_0 \end{cases} \tag{12}$$

where $x > x_0$ is defined as the damping region; L_s refers to the length of damping region; and a_s refers to the wave-absorbing coefficient.

4. Numerical Modelling

4.1. Computational Domain and Boundary Conditions

Since the hull model is symmetrical with respect to the mid-longitudinal section, the numerical modeling can be taken in half, with the advantage of saving computing resources and time. For different simulations with calm water and regular waves, the ranges of the background domain were set to be consistent in the y and z directions, and the domain extended from $-1.5 < y/L < 0$, $-1.5 < z/L < 0.5$. The size of the domain was different for the two type cases in the x direction, in which $-4 < x/L < 1$ for the calm water and $-3 < x/L < 1$ for the regular waves. The reduced distance for the regular waves aimed to reduce the number of meshes and save computing resources.

The boundary conditions were set as follows: the velocity inlet boundary conditions were applied on the front, top, and bottom of the background domain; the pressure outlet boundary condition was applied on the end of the background domain; two sides were set as the symmetry boundary condition; three surfaces of the overset domain were set as the overset mesh boundary condition; and the surfaces of the hull were set as the non-slip boundary condition. The computational domain and boundary conditions are shown in Figure 5.

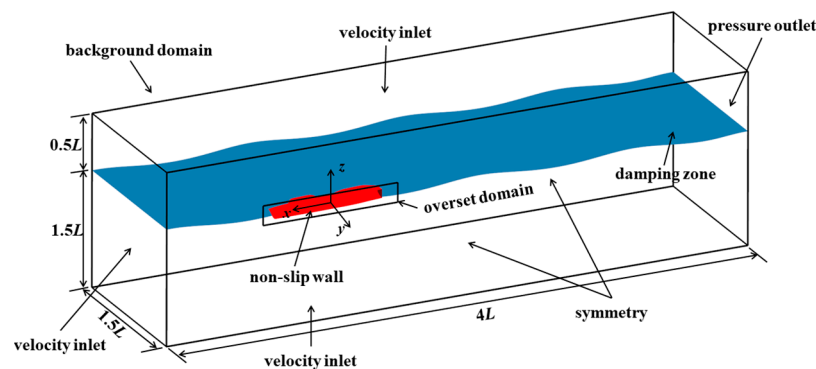


Figure 5. The computational domain and boundary conditions.

4.2. Mesh Generation

Mesh is a very important aspect of numerical simulation and one of the most time-consuming processes. The quality of the mesh directly affects the accuracy and efficiency of CFD simulations. The fully structured overset mesh was applied in the present study, which can be divided into two parts before the overset: background mesh and overset mesh. The two parts were both generated as trimmed-type topology. For wave problems,

the number of meshes of the free surface is the key factor for the accuracy of the numerical simulation. In the mesh division of free surface, 10~20 layers of meshes in one wave height and 30~50 layers of meshes in one wavelength are needed. The mesh size ratio of element mesh in wave region in x , y , and z directions was 2:2:1. In order to ensure the accuracy of the overset mesh in the interpolation calculation, the y^+ value of wall grid was between 30 and 300. The background meshes were also encrypted in the region where the overset mesh pitches and sinks, which occupied a large part of the number of meshes and increased the calculation time. Figure 6 shows the mesh division in the wave condition.

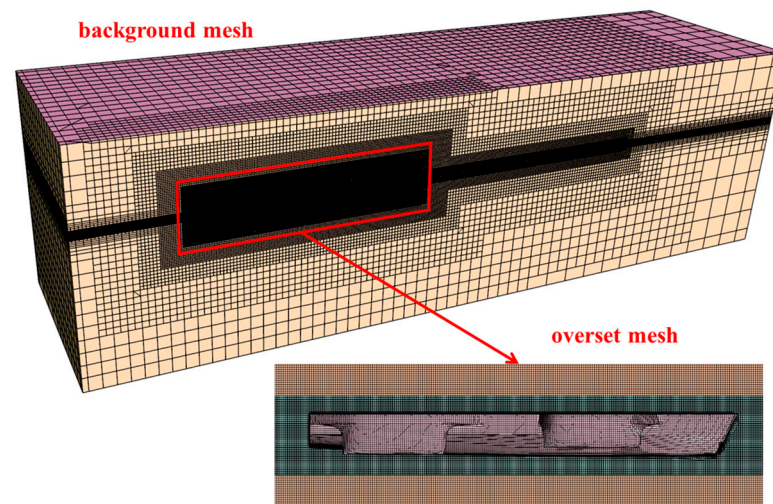


Figure 6. The background mesh and overset mesh of the pentamaran in the wave condition.

For the computations in calm water, only a certain degree of mesh refinement was required in the Kelvin wave region behind the stern to capture the Kelvin wave system. For the computations in waves, further refinement of the meshes near the free surface occurred in order to better simulate the incoming regular waves. More than 50 cells per wave length and 15 cells per wave height were used. Prism layers were applied on the hull surface, making the y^+ range from 100 to 300 according to the ITTC recommendation [48]. Figure 7 shows the horizontal section of the mesh in calm water and waves. The mesh size of the monohull and pentamaran surface was 0.1 m. The mesh size of the free surface in the z direction was 0.1 m. The total mesh number in calm water and waves is listed in Table 6.

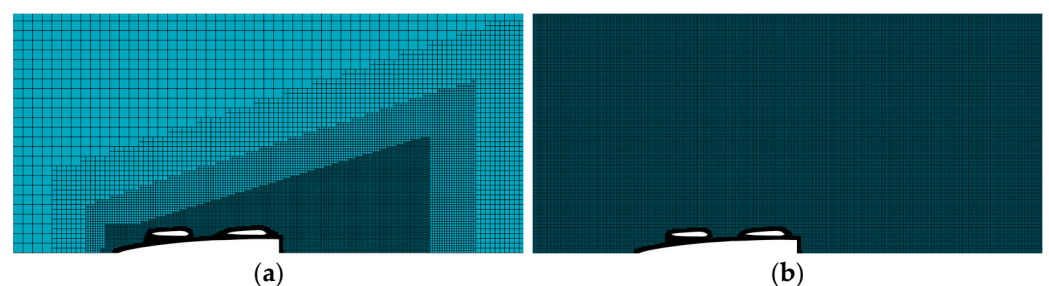


Figure 7. Horizontal section of the mesh: (a) calm water condition; (b) wave condition.

Table 6. Mesh number in calm water and waves.

Simulations	Background	Overset	Total
Calm water	2,697,325	681,023	3,378,348
Regular waves	5,901,263	681,713	6,582,976

The time step size was 0.01 s, and the convective courant number was 1.25. At the beginning of the calculation, the flow field was relatively rough, and a small time step was

used to control the range of the courant number between 0.5 and 1. When the calculation was relatively stable, the time step size and the courant number could be increased to save the calculation time.

4.3. Validation of the Numerical Method

To evaluate the reliability of the numerical method, it is necessary to validate the numerical model. One of the best ways to do this is to compare simulation data with experimental data. However, there are no relevant test data applicable to the pentamaran or monohull. Another method is to carry out numerical simulations of the standard hull model, which can also prove the reliability of the numerical method. KCS is a modern container ship designed by KRISO (Koera Research Institute of Ship and Ocean Engineering) in Korea and was listed as one of the standard ship types for CFD assessment and verification in the Gothenburg-2000 conference [43]. The KCS ship model has a large bulbous bow and a complex tail surface, belonging to the hypertrophy ship category [49]. The main particulars and the geometry of the full-scale monohull are shown in Figure 8 and Table 7, respectively.



Figure 8. The geometry of the KCS model.

Table 7. Main particulars of the monohull.

Particulars	Symbols/Unit	Value
Scaling ratio	λ	31.60
Length between perpendiculars	L_{pp}/m	7.278
Breadth	B_{wl}/m	1.01
Molded depth	D/m	0.60
Draft	d/m	0.341
Displacement	∇/m^3	1.649
Wetter area	S/m^2	9.512
Waterline coefficient	C_w	0.818
Block coefficient	C_b	0.65

The total mesh number was 3,000,000. Figure 9 shows the section of the mesh and the mesh at the bow and stern.

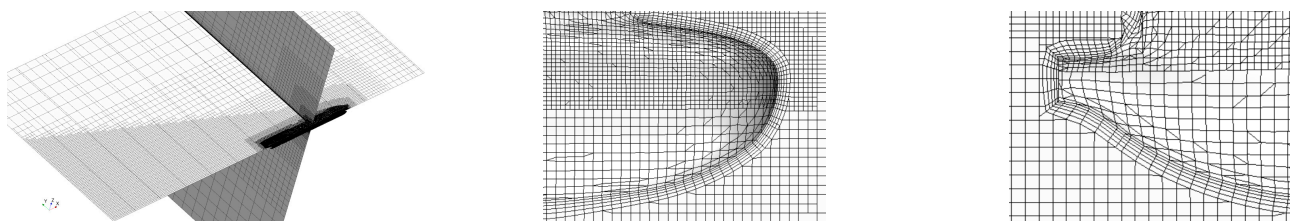


Figure 9. The KCS mesh.

For the computations in calm water, six conditions were selected in the range of low and medium speeds. The validation objects were total resistance coefficient, heave, and pitch. The total resistance coefficient was calculated as follows:

$$C_t = \frac{R_t}{0.5\rho U^2 S} \tag{13}$$

where C_t is the total resistance coefficient, R_t is the total resistance, ρ is the density of water, U is the speed, and S is the wetted area of the hull. This is the same as C_p and C_f .

Figure 10 shows the simulation results of the total resistance coefficient of KCS at different speeds. The simulation results are in good agreement with the experimental data. Among the six calculation conditions, the largest error 2.29% occurred at $F_n = 0.108$, which was due to the difficulty of resistance convergence at low speed. When the speed was high, the simulation results were in good agreement with the experimental values. From the changing trend, the resistance coefficient first decreased with the increase in the speed, and then increased rapidly after reaching the condition of $F_n = 0.195$.

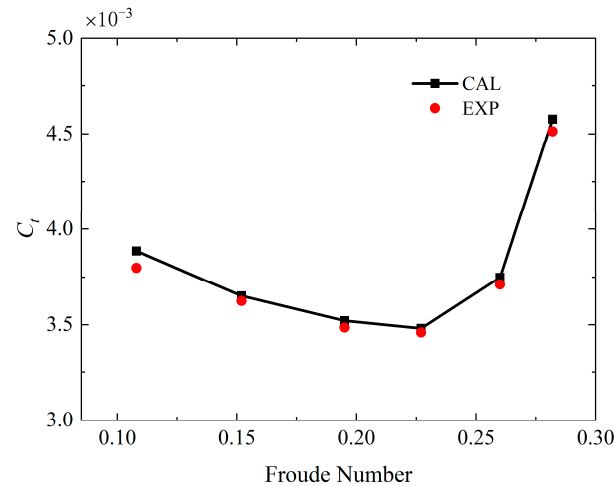


Figure 10. Comparison of total resistance coefficients of KCS.

Figure 11 shows the comparison of the hull motions of KCS between the simulation results and experimental data. The heave and pitch values were generally similar to the experimental data. From the changing trend, the heave value increased with the increase in the speeds, and the growth rate also increased. The pitch value first increased in the direction of the negative value (stern inclination), reached the maximum value in the negative direction at $F_n = 0.26$, and then changed in the direction of the positive value.

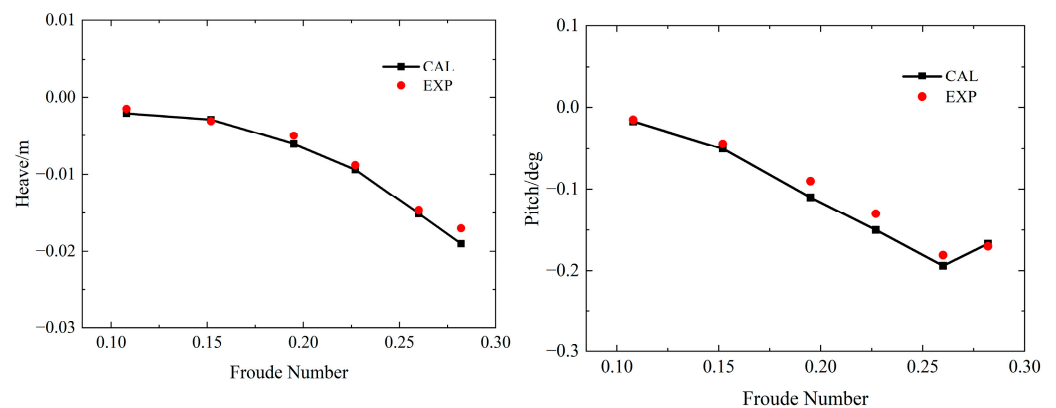


Figure 11. Comparison of heave and pitch of KCS.

The global view of the wave pattern of the KCS at $F_n = 0.26$ is shown in Figure 12. Compared with the experimental result, the calculated waveform was in good agreement with the experimental waveform in terms of wavelength and wave shape. The VOF method used in numerical simulation can accurately capture Kelvin waves for large ships. It should be noted that only the starboard side was measured and reflected on the port side for plotting. It was observed that a wave existed inside a certain angle known as the Kelvin angle from linear potential wave theory. The bow wave, having the maximum height on the hull surface, gradually disappeared, followed by a trough and crest lines of divergent wave

components with decreasing amplitude along the edge of the wave region. Transverse wave components were seen inside the divergent wave patterns.

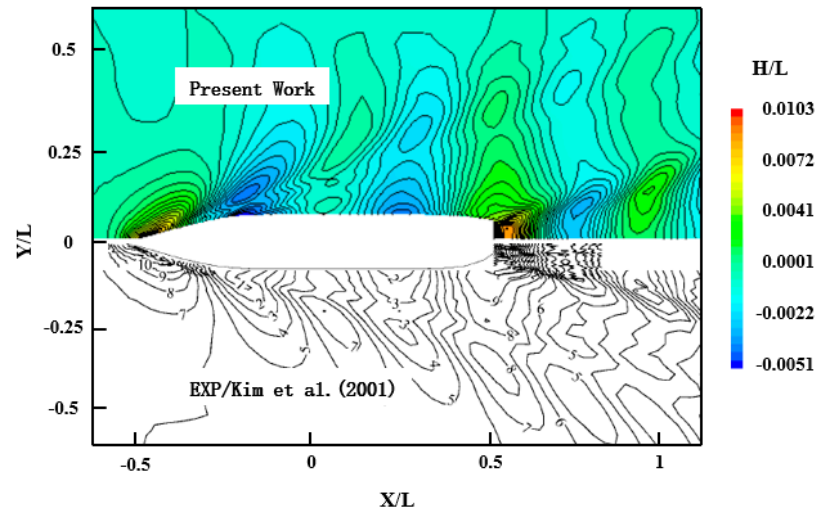


Figure 12. The wave pattern at $F_n = 0.26$ [49].

For the computations in waves, with reference to the work of Zhang et al. [50], the wave height a was 0.123 m, the wavelength L was $1.15 L_{pp}$, the speed $F_n = 0.26$, and the wave model was the fifth-order Stokes wave. The validation objects were added resistance, heave, and pitch. Since the motion and resistance of the hull in waves are periodic, for the convenience of comparison, Fourier transform was performed on the motion and force of the hull. The added resistance and motion of KCS in waves were compared with the experimental data, as shown in Table 8.

Table 8. Comparison of added resistance and motion of KCS in waves with experimental data.

Item	CFD	Experiment	Error
C_{aw}	10.9	10.0	9.00%
Heave/mm	49.7	55.4	−10.28%
Pitch/deg	2.64	2.38	10.92%

$$C_{aw} = \frac{\bar{R}_{aw} - R_{calm}}{(\rho g a^2 B)/L_{pp}}; \text{Error} = (\text{CFD} - \text{EXP})/\text{EXP}.$$

It can be seen from Table 8 that the simulation results of resistance in waves was relatively close to the experimental data, but the accuracy was lower than that of the calm water condition, especially the error of ship motion, which was slightly larger. The reason may have been that there was strong mutual interference between the ship model wave-making and incoming waves in waves, and the nonlinearity in the simulation was greatly increased, with the amplitude of the motion in the waves being high-order, so the calculation accuracy was greatly challenged. However, on the whole, the simulations were able to reflect the motion characteristics and force of the ship.

Figure 13 shows the wave pattern at typical time in regular waves. The wave pattern in regular waves was well captured. When the KCS hull sailed in waves, in addition to the ship traveling waves related to the sailing speed and water depth, another wave related to the hull motion induced by the incident waves was also generated. These two kinds of waves will consume the energy of the hull and superimpose each other, so the energy consumed by the ship when sailing in waves will be higher than that in still water, and the additional energy loss is the so-called added resistance.

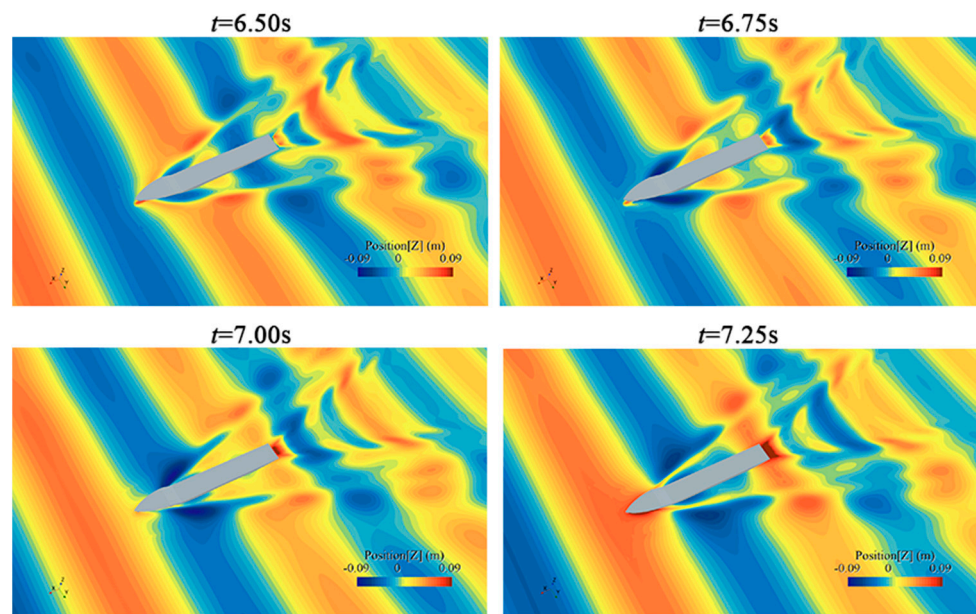


Figure 13. The wave pattern at typical time in regular waves.

In general, the simulation results of KCS were in good agreement with the experimental results. Through the numerical simulation of KCS in calm water and regular waves, the reliability of the numerical method in this paper was verified.

5. Results and Discussions

5.1. Hydrodynamic Performance in Calm Water

In this section, the hydrodynamic performance of the pentamaran in calm water is discussed and compared with the monohull, including the resistance performance, degrees of freedom, the wave pattern, and the streamline distribution.

5.1.1. Resistance Performance

According to the direction of force, the total resistance can be divided into pressure resistance R_p and friction resistance R_f . Pressure resistance R_p is the force acting on the hull surface vertically caused by wave making and vortex. The calculation results of R_p and C_p under five cases are shown in Table 9 and Figure 14.

Table 9. Calculation results of pressure resistance.

Case	R_p/N		$C_p \times 10^3$	
	Monohull	Pentamaran	Monohull	Pentamaran
1	773.8	1511.4	3.238	4.183
2	2519.0	4633.0	2.635	3.206
3	5920.2	8892.8	2.752	2.735
4	10,859.6	14,553.4	2.840	2.517
5	16,319.4	21,816.0	2.731	2.415

It can be known from Table 9 and Figure 14 that

(1) The change trends of the R_p curve of the monohull and the pentamaran were basically the same. The difference of R_p increased with the increase in the speed. Under case 1 and case 2, the pressure resistance of the pentamaran was about twice that of the monohull. With the increase in the speed, the increment of the pressure resistance of the pentamaran relative to the monohull was about 1/3 of that of the monohull. The C_p of the monohull decreased significantly, while the C_p of the pentamaran was always in a downward state. Both had the same value at the speed of 15 kn.

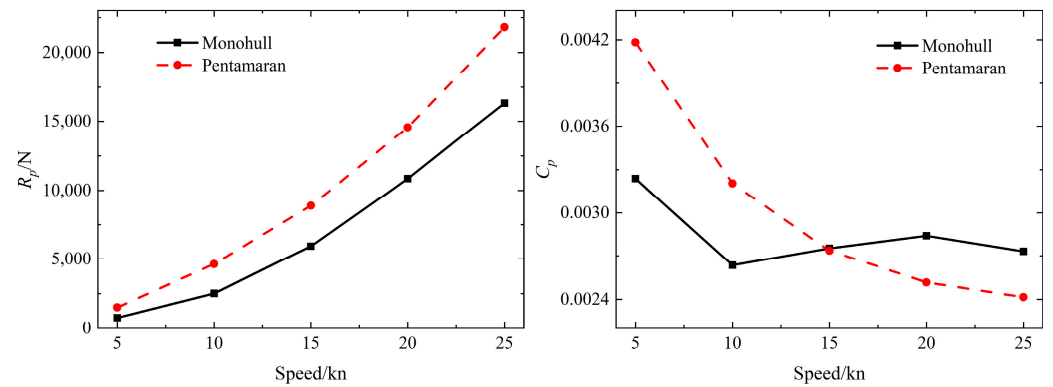


Figure 14. R_p and C_p curves.

(2) The C_p is a dimensionless dimension of R_p , which mainly depends on the pressure difference between the bow and stern, and it can reflect the wave-making ability of the hull to a certain extent. In the medium-speed range, the C_p of the pentamaran was larger than that of the monohull, indicating that the wave-making ability of the pentamaran was weaker than that of the monohull. It was preliminarily inferred that the waves arising from the side hulls and the main hull were superimposed on each other, resulting in unfavorable interference. In the high-speed range, the C_p of the pentamaran was slightly lower than that of the monohull, indicating that the waves arising from the side hulls and the main hull at this time had favorable interference.

In conclusion, the calculation results show that whether it was a monohull or a pentamaran, the speed change had a significant impact on the C_p . The pentamaran may have better wave-making performance than the monohull in high-speed range.

The friction resistance R_f is the tangential force of the water point along the hull surface, which is mainly affected by the wetted surface area. The calculated values of R_f and C_f under five cases are shown in Table 10 and Figure 15.

Table 10. Calculation results of pressure resistance.

Case	R_f/N		$C_f \times 10^3$	
	Monohull	Pentamaran	Monohull	Pentamaran
1	539.0	840.0	2.256	2.325
2	1875.2	3260.6	1.961	2.256
3	3950.8	6859.8	1.837	2.109
4	6459.0	11,848.6	1.689	2.049
5	9659.6	18,036.8	1.617	1.997

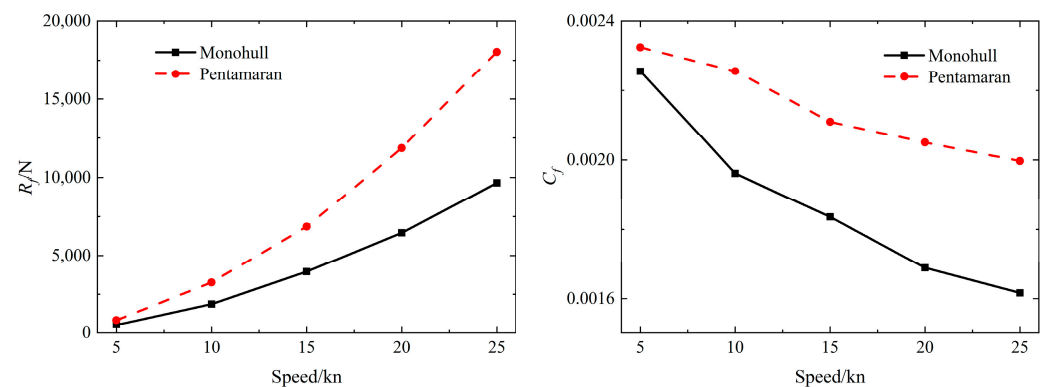


Figure 15. R_f and C_f curves.

It can be known from Table 10 and Figure 15 that

(1) The R_f of the pentamaran was always about twice that of the monohull. There was little difference between the two in the low-speed range. The difference was obvious in the high-speed range.

(2) The C_f of the pentamaran was always greater than that of the monohull. It is worth noting that the C_f curve of the monohull showed a significant downward curve in the entire speed range, while the downward trend of the pentamaran was relatively slow. Considering that the hull model used in this paper was a high-speed shuttle hull, the reason for this phenomenon was preliminarily inferred as follows: due to the addition of two front hulls, the pentamaran had a smaller tilting motion than the monohull at medium and high speeds, and the immersion area of the pentamaran at high speed was larger than that of the monohull.

In conclusion, the calculation results show that the side hulls had an adverse effect on the friction resistance of the pentamaran.

Total resistance R_t is the sum of R_p and R_f . The calculated values of R_t and C_t under five cases are shown in Table 11 and Figure 16.

Table 11. Calculation results of pressure resistance.

Case	R_f/N		$C_f \times 10^3$	
	Monohull	Pentamaran	Monohull	Pentamaran
1	1312.8	2351.4	5.349	6.508
2	4394.2	7893.6	4.596	5.461
3	9871.0	15,752.6	4.589	4.844
4	17,318.6	26,402.0	4.529	4.567
5	25,979.0	39,852.8	4.348	4.412

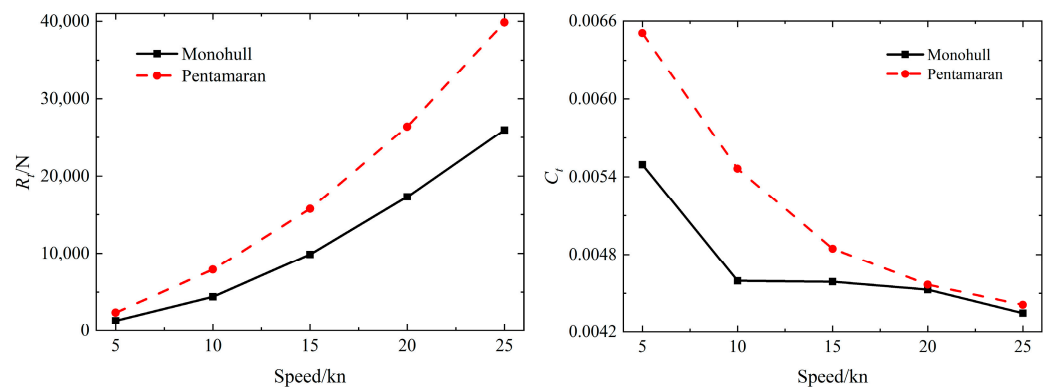


Figure 16. R_t and C_t curves.

5.1.2. Degrees of Freedom

The calculated heave and pitch values of the monohull and pentamaran under five cases are shown in Figure 17.

It can be known from Figure 17 that

(1) The variation trend of the heave values of the two ship types was the same, which increased with the increase in the speeds. The difference was that the heave values of the monohull were increasing from a positive value, while that of the pentamaran were increasing from a negative value, indicating that the pentamaran will sink slightly in the low-speed range. The heave values of the monohull were always greater than that of the pentamaran, indicating that the wetted area was smaller than that of the pentamaran, resulting in the friction resistance of the monohull being smaller than that of the pentamaran.

(2) Both ship types were unable to produce a large pitch angle at low speed, and the difference between the two was not large. With the increase in the speeds, the stern of the

pentamaran was smaller than that of the monohull, and the difference increased with the increase in the speeds.

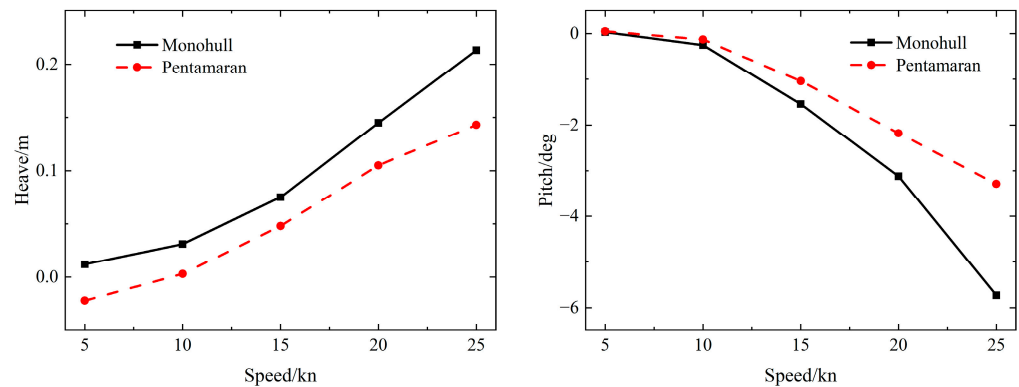


Figure 17. Heave and pitch in calm water.

The results of heave and pitch further proved the above inference on the friction resistance: although the motion of the pentamaran was gentler than that of the monohull, it would also increase the friction resistance of the pentamaran.

5.1.3. Wave Pattern

Figure 18 shows the wave patterns of monohull and pentamaran in calm water. It can be known from Figure 18 that

(1) At a low speed of 5 kn, there were two obvious Kelvin wave patterns at the bow and stern of the monohull, and there was almost no wave interference in the middle section of the hull. The Kelvin wave generated by the side hulls of the pentamaran was fused and superimposed with the bow and stern, forming a longer scattered wave. At the speed of 10 kn, the Kelvin wave pattern of the pentamaran was significantly larger than that of the monohull. Wave peaks were generated between the front hulls and the main hull, and the wave peaks generated by the head of the rear hulls and the main hull were superimposed, which was uncondusive to wave-making resistance. The wave trough at the stern of a catamaran is larger than that of a monohull, and the range of wave peaks after the stern is reduced.

(2) At medium and high speeds of 15 kn, 20 kn, and 25 kn, there was almost no wave making in the inflow area in front of the bow of the two ship types, which was related to the special bow shape of the monohull, and its bow was thin and pointed. There was a cock-tail flow in the tail area, which was divided into two strands at the rear area, and the cock-tail was formed into an arrow shape. Due to the installation of the side hulls, the wave trough generated by the main hull at the position of the side hulls met the side hulls, which would cancel each other out with the wave crest generated by the side hulls, thereby causing the trough area to move backwards. In addition, the waves generated at the tail of the rear side hulls and the waves generated at the tail of the main hull were coupled to each other to form multiple wave valleys, which reduced the wave crest area behind the stern.

In conclusion, the wave patterns of the monohull and pentamaran in calm water show that the waves between the side hulls and the main hull of the pentamaran superimposed each other at low speeds, resulting in unfavorable interference and wave resistance. At medium and high speeds, the range of the wave crest at the stern of the pentamaran was reduced, and the range of the wave trough was increased. The wave-making of the rear side hulls was able to offset part of the waves of the main hull. The impact of the front hulls on the wave-making of the main hull was small. The influence of the rear hulls on the wave-making was mainly reflected in the wave valley area.

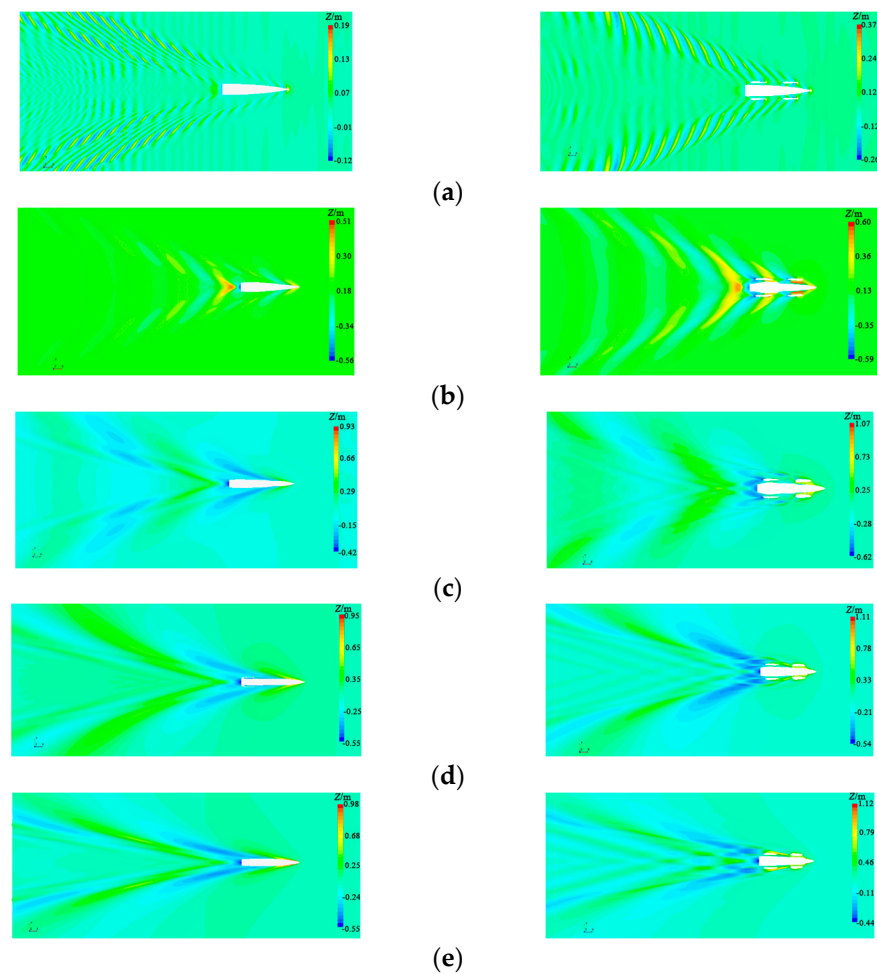


Figure 18. The wave patterns of monohull (left) and pentamaran (right) in calm water: (a) case 1; (b) case 2; (c) case 3; (d) case 4; (e) case 5.

5.1.4. Streamline Distribution

Figure 19 shows the streamline distribution of the monohull and pentamaran in calm water. Streamlines were rendered with a pressure function. It can be known from Figure 19 that the distribution of the head streamlines did not change much under different cases. Because of the transom stern, the streamline was disordered when the speed was high. When the streamline flowed through the transom stern, it shrunk inwards, resulting in a turbulent vortex at the stern of the monohull under cases 2 and 4. The streamlines at the stern of the pentamaran under the same cases were more regular, indicating that the rear hulls had a rectification effect.

5.2. Hydrodynamic Performance in Regular Waves

In this section, the hydrodynamic performance of the pentamaran in regular waves is discussed and compared with the monohull, including the resistance performance, ship motion response, and the wave patterns.

5.2.1. Resistance Performance

For calculations in waves, the model remained positive floating at the initial time. The degree of freedom of the hull was released after 0.5 s. The total physical time was 20 s.

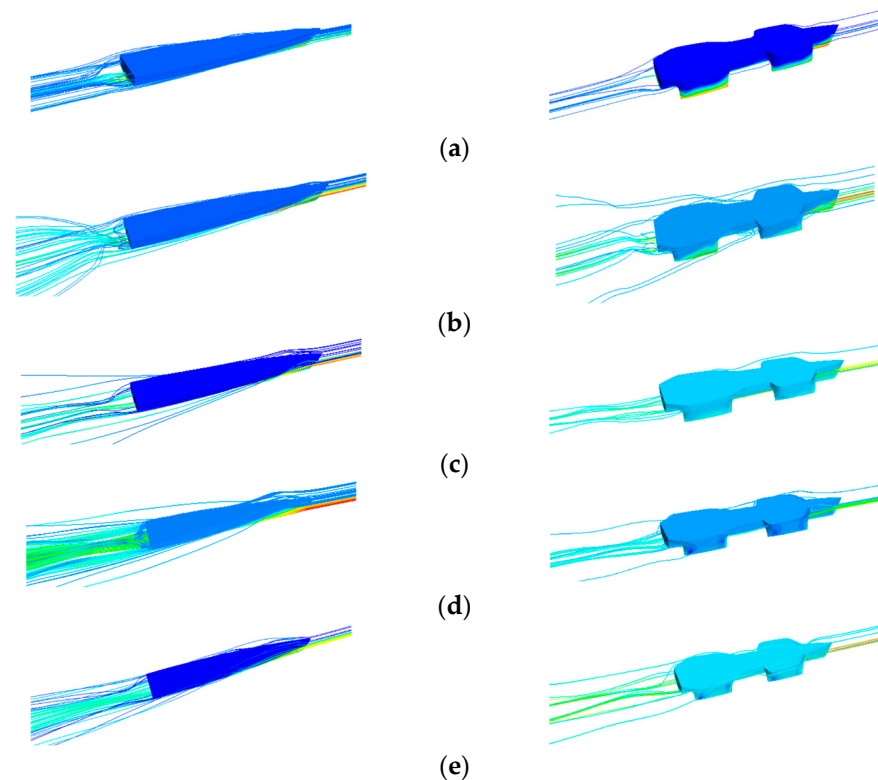


Figure 19. The streamline distribution of the monohull (left) and pentamaran (right) in calm water: (a) case 1; (b) case 2; (c) case 3; (d) case 4; (e) case 5.

Figure 20 shows the time history curve of total resistance under case 6. The horizontal axis represents the physical time, the vertical axis represents the total resistance, and the dotted line represents the total resistance in calm water. It can be known from Figure 20 that

(1) When sailing in the regular head waves, the total resistance of the monohull and pentamaran showed obvious periodic changes.

(2) When the wave period was π , the change trend of the total resistance of the monohull ship was relatively intense, and the time history curve of the total resistance was not a regular positive (cosine) chord curve, indicating that the total resistance of the monohull was strongly nonlinear under such wave conditions. The change trend of the total resistance of the pentamaran was slower than that of the monohull, and the time-history curve of the total resistance was a relatively regular sine (cosine) wave, indicating that the total resistance of the pentamaran was linear under such wave conditions.

(3) Compared with the resistance in calm water, the total resistance of the monohull was smaller most of the time in an encounter cycle, while the pentamaran showed the opposite trend. It was preliminarily speculated that due to the additional four side hulls, the total weight of the pentamaran was heavier than that of the monohull, the hulls sunk in the wave, the trim range in the wave was smaller, and the wetted area increased.

Figure 21 shows the time history curve of total resistance under case 7. The horizontal axis represents the physical time, the vertical axis represents the total resistance, and the dotted line represents the total resistance in calm water. It can be known from Figure 21 that when the wave period changed from π to $\pi/2$, the amplitude and frequency of the total resistance curve of the monohull did not change significantly. The amplitude of the total resistance of the pentamaran decreased from about 18,500 N to about 10,000 N. This showed that as the wave period became shorter, the resistance increment of the pentamaran became smaller in the wave.

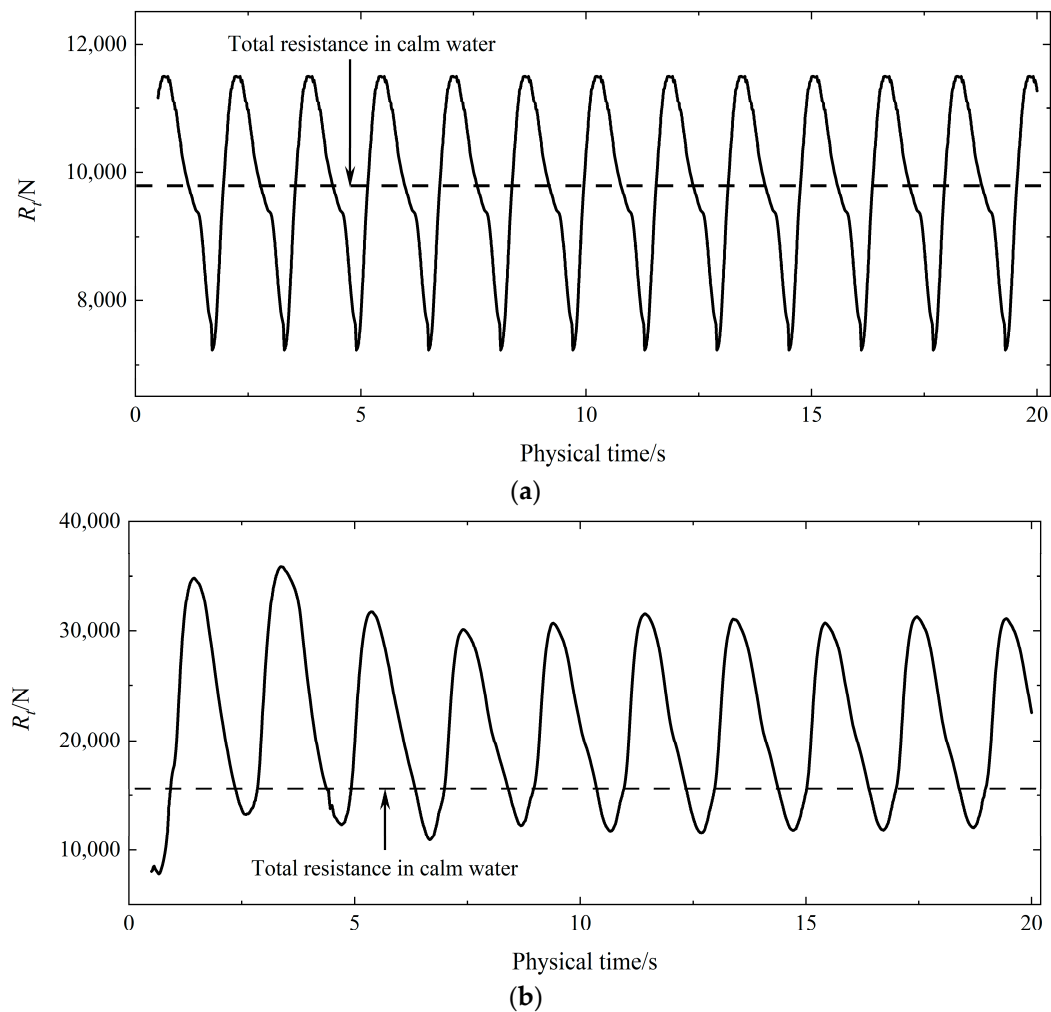


Figure 20. The time history curve of total resistance under case 6: (a) monohull; (b) pentamaran.

In conclusion, the calculation results show that the total resistance of the monohull oscillated near the calm water resistance, while the total resistance of the pentamaran was in an increasing state most of the time in an encounter cycle. The total resistance of the pentamaran was more affected by the wave period (wavelength). As the wave period became shorter, it developed in the direction that was conducive to drag reduction.

5.2.2. Ship Motion Response

Figures 22 and 23 show the heave motion of the monohull and pentamaran under cases 6 and 7. The horizontal axis represents the physical time, and the vertical axis represents the heave amplitude. Negative heave amplitude means the hull sinks. It can be known from Figures 22 and 23 that

(1) Under wave conditions, the heave amplitudes of the monohull and pentamaran both showed periodic changes. The difference was that the heave of the monohull could be positive or negative, while the heave of the pentamaran was always negative, which indicates that the side hulls would sink the whole ship during wave navigation. It proves the conclusion that the resistance of the pentamaran increases in most encounter cycles.

(2) When the wave period changed from π to $\pi/2$, the heave amplitude of the monohull and pentahull decreased, which indicates that the shorter the wavelength, the smaller the heave amplitude of the hull.

(3) No matter the wave period being π or $\pi/2$, the heave amplitude of the pentamaran was always smaller than that of the monohull, which indicated that the navigation state of the pentamaran in the waves was more stable than that of the monohull.

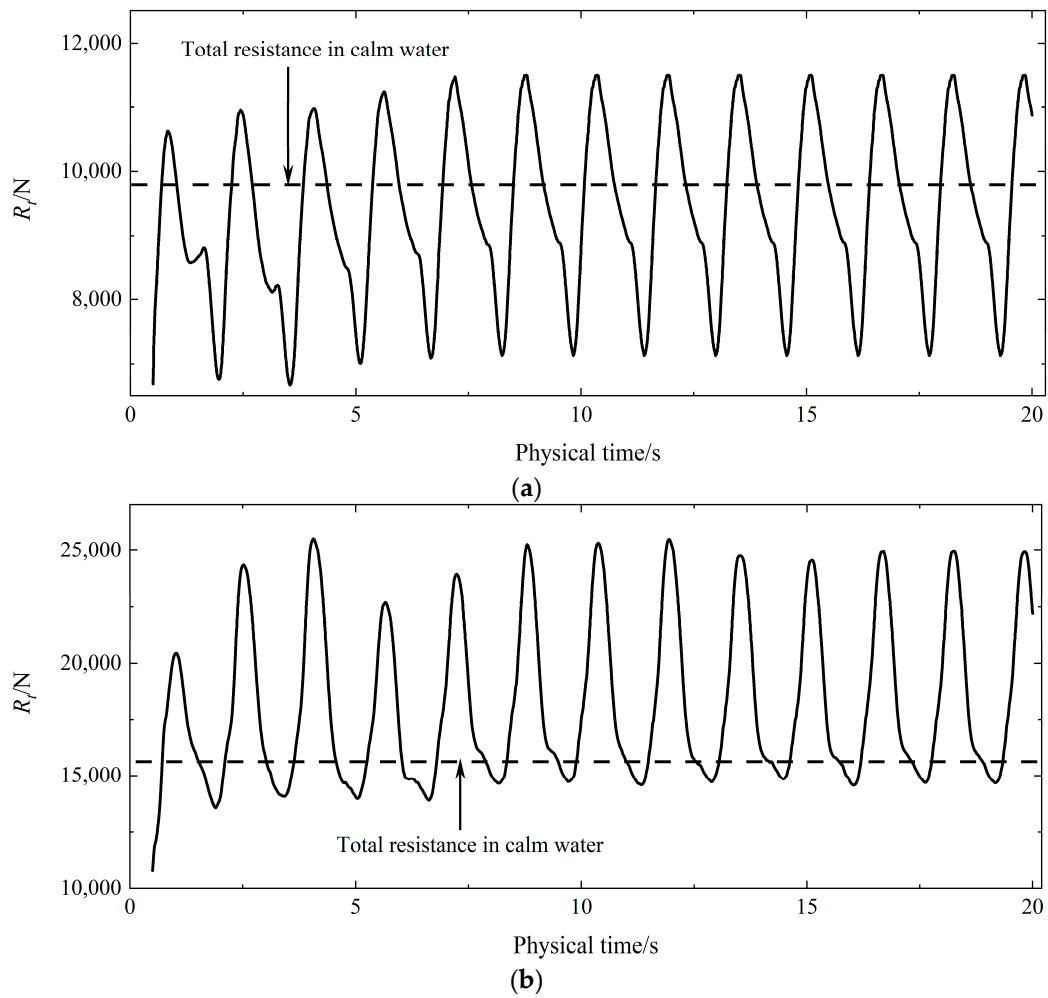


Figure 21. The time history curve of total resistance under case 7: (a) monohull; (b) pentamaran.

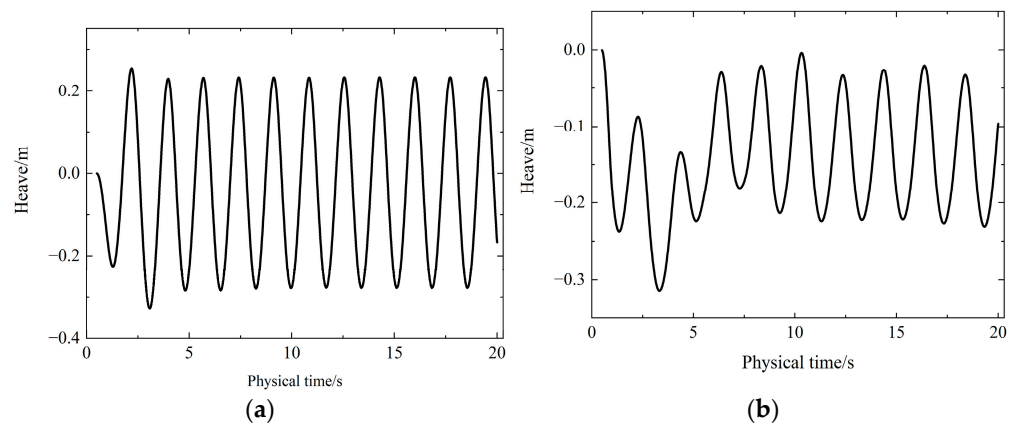


Figure 22. The time history curve of heave amplitude under case 6: (a) monohull; (b) pentamaran.

Figures 24 and 25 show the pitch motion of the monohull and pentamaran under cases 6 and 7. The horizontal axis represents the physical time, and the vertical axis represents the pitch angle. Negative pitch angle means the hull is tilted towards the stern. It can be known from Figures 24 and 25 that

(1) Under the same wave period, the pitch motion amplitude of the pentamaran was smaller than that of the monohull, the bow inclination of the two types of hulls was not

much different, and the stern inclination of the pentamaran was slightly smaller than that of the monohull.

(2) When the wave period changed from π to $\pi/2$, the stern inclination of both monohull and pentamaran decreased, indicating that the shorter the wavelength, the smaller the trim amplitude of the hull.

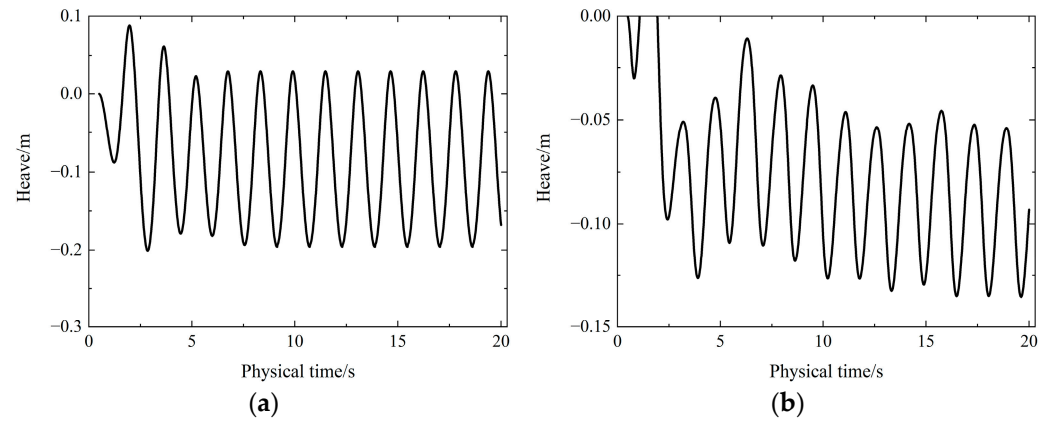


Figure 23. The time history curve of heave amplitude under case 7: (a) monohull; (b) pentamaran.

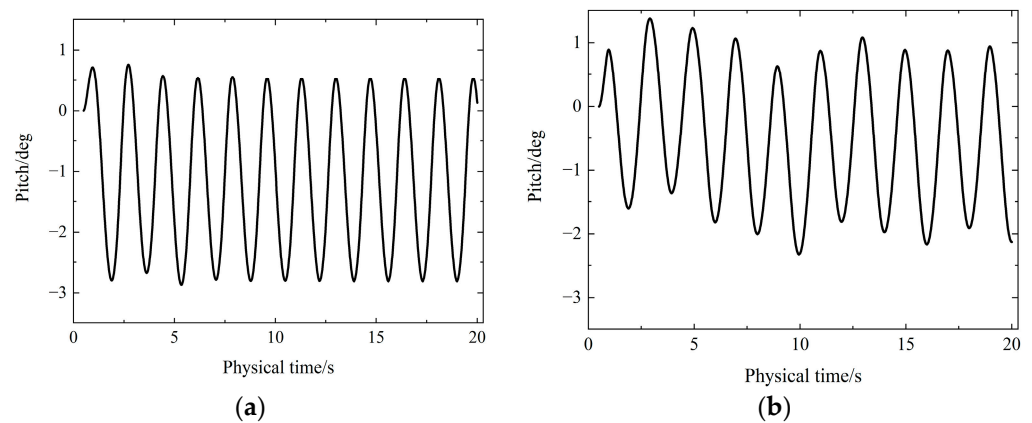


Figure 24. The time history curve of pitch angle under case 6: (a) monohull; (b) pentamaran.

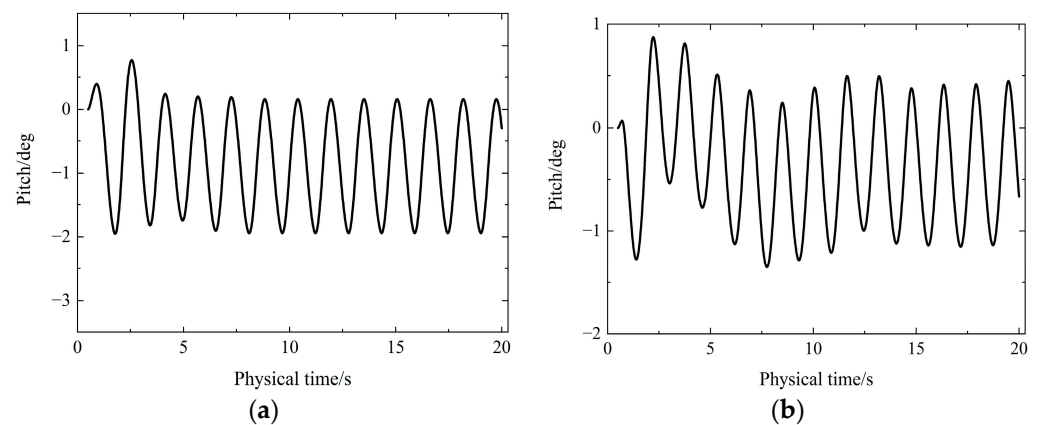


Figure 25. The time history curve of pitch angle under case 7: (a) monohull; (b) pentamaran.

In conclusion, the calculation results show that the motion response of the monohull was more severe than that of the pentamaran in regular waves, and the pentamaran was more stable in regular waves.

5.2.3. Wave Pattern

From the above analysis, it can be seen that both the monohull and pentamaran had a certain periodicity in navigation. Therefore, this paper selected two states of bow encountering a wave crest and bow encountering a wave trough to show the situation of the wave pattern. Figures 26 and 27 show the wave patterns in regular waves. It can be known from Figures 26 and 27 that

(1) When the wave crest reached the bow, the wave breaking phenomenon was the most obvious at this time, and the bow draft was relatively serious. When the wave trough reached the bow, the bow draft increased slightly, and the whole free surface was relatively relaxed.

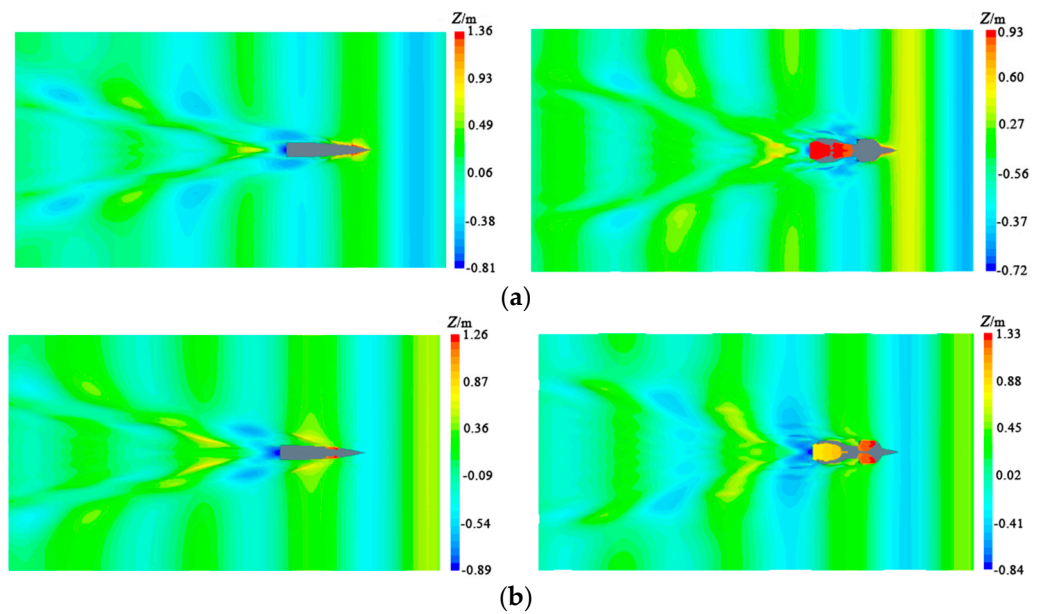


Figure 26. The wave patterns of the monohull and pentamaran in regular waves under case 1: (a) bow encounters a wave crest; (b) bow encounters a wave trough.

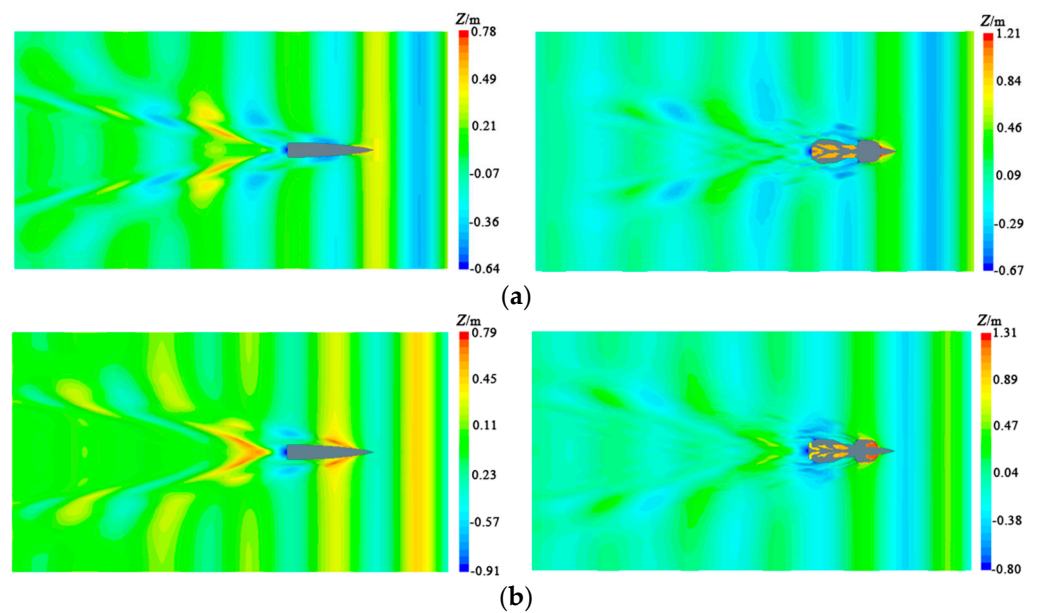


Figure 27. The wave patterns of the monohull and pentamaran in regular waves under case 2: (a) bow encounters a wave crest; (b) bow encounters a wave trough.

(2) Under long waves with a wave period of π , there was a large area of waves on the deck of the pentamaran, and the resistance of the pentamaran showed relatively strong nonlinearity. When the wave period changed from π to $\pi/2$, the wave area on the deck decreased.

6. Conclusions

In this paper, the hydrodynamic performance of a monohull and a pentamaran was numerically simulated in calm water and regular waves. The RANS equation was solved on the basis of the finite volume method. The resistance prediction of the pentamaran in calm water and regular waves was completed, and the changes of each resistance component compared with monohull were explored. This paper draws the following conclusions:

(1) In calm water, the adverse effect of the side hulls on the resistance is mainly reflected in the low-speed range. In the high-speed range, the influence of the side hulls on the resistance can be ignored. At high speeds, the main hull and side hulls of the pentamaran will produce favorable wave-making interference, thereby improving the wave-making performance of the pentamaran.

(2) The side hulls have a great influence on the pressure resistance but have no obvious influence on the friction resistance. The rear hulls can rectify the tail flow field.

(3) In regular waves, although the added resistance of the pentamaran is increasing most of the time, its amplitude is smaller than that of the monohull under the same wave condition. The shorter the wave period, the more obvious this conclusion.

(4) The amplitude of heave motion and pitch angle of the pentamaran in waves are less than that of monohull, which shows that the pentamaran is more stable in wave navigation, and its seakeeping performance is better than that of a monohull ship in the same scale.

(5) It is worth noting that the pentamaran is always in a state of sinking during wave navigation. The phenomenon of rising waves on the deck frequently occurs, and the area of rising waves is large. Therefore, in the design of the pentamaran, the main dimensions, speed, water environment, and the wave phenomenon on the deck should be comprehensively considered.

Author Contributions: Conceptualization, D.Z. and B.Z.; methodology, D.Z. and H.J.; software, J.S.; validation, D.Z. and B.Z.; formal analysis, D.Z. and B.Z.; investigation, J.S. and B.Z.; resources, D.Z.; data curation, J.S.; writing—original draft preparation, D.Z.; writing—review and editing, D.Z.; visualization, J.S. and B.Z.; supervision, D.Z. and J.S.; funding acquisition, D.Z. and H.J. All authors have read and agreed to the published version of the manuscript.

Funding: This research was funded by Program for Scientific Research Start-up Funds of Guangdong Ocean University, grant number 060302072101; Zhanjiang Marine Youth Talent Project- Comparative Study and Optimization of Horizontal Lifting of Subsea Pipeline, grant number 2021E5011; and the National Natural Science Foundation of China, grant number 62272109.

Institutional Review Board Statement: Not applicable.

Informed Consent Statement: Not applicable.

Data Availability Statement: Not applicable.

Conflicts of Interest: The authors declare no conflict of interest.

References

1. Corbett, J.J.; Wang, H.; Winebrake, J.J. The effectiveness and costs of speed reductions on emissions from international shipping. *Trans. Res. Part D Trans. Environ.* **2009**, *14*, 593–598. [[CrossRef](#)]
2. Taskar, B.; Andersen, P. Benefit of speed reduction for ships in different weather conditions. *Trans. Res. Part D Trans. Environ.* **2020**, *85*, 102337. [[CrossRef](#)]
3. Banawan, A.A.; Mosleh, M.; Seddiek, I.S. Prediction of the fuel saving and emissions reduction by decreasing speed of a catamaran. *J. Mar. Eng. Technol.* **2013**, *12*, 40–48.
4. Zis, T.; North, R.J.; Angeloudis, P.; Ochieng, W.Y.; Harrison Bell, M.G. Evaluation of cold ironing and speed reduction policies to reduce ship emissions near and at ports. *Marit. Econ. Logist* **2014**, *16*, 371–398. [[CrossRef](#)]

5. Begovic, E.; Bertorello, C.; Caldarella, S.; Cassella, P. *Pentamaran Hull for Medium Size Fast Ferries*; Hydrodynamics VI; Taylor Francis Group: Abingdon, UK, 2004; pp. 23–28.
6. Luhulima, R.B.; Alia, M.R.; Utama, I. Experimental Investigation into the Resistance Characteristics of Trimaran and Pentamaran Configurations. *Int. J. Technol.* **2021**, *12*, 1058–1070. [[CrossRef](#)]
7. Gee, N.; Dudson, E.; Marchant, A.; Steiger, H. The pentamaran—a new hull concept for fast freight and car ferry applications. In Proceedings of the 13th Fast Ferry International Conference, Singapore, 25–27 February 1997.
8. Gee, N.; Dudson, E.; González, J.M. The IZAR Pentamaran—Tank Testing, Speed Loss and Parametric Rolling. 2009. Available online: <https://bmtmarketing.azureedge.net/media/2400/paper21.pdf> (accessed on 27 March 2023).
9. Dudson, E.; Harries, S. Hydrodynamic fine-tuning of a pentamaran for high-speed sea transportation services. In Proceedings of the 8th International Conference on Fast Sea Transportation (FAST 2005), Saint Petersburg, Russia, 27–30 June 2005.
10. Wu, M.; Moan, T. Numerical prediction of wave-induced long-term extreme load effects in a flexible high-speed pentamaran. *J. Mar. Sci. Technol.-Jpn.* **2006**, *11*, 39–51. [[CrossRef](#)]
11. He, J.S.; Zhang, F.X.; Chen, Z.; Xiao, X. An experimental study on pentamaran resistance characteristic. *J. Shanghaijiaotong Univ.* **2007**, *41*, 1449–1453.
12. Duan, Y.X.; Lu, X.P.; Wang, Y.; He, L. Calculation of wave resistance by linear theory and CFD simulation for pentamaran. *Chin. J. Ship Res.* **2011**, *6*, 1–7. (In Chinese)
13. Duan, Y.X.; Liu, Y.; Wang, Y.; Tang, G.L. Research on the demihulls layout and wave resistance optimization of pentamaran. *Ship Sci. Technol.* **2015**, *37*, 10–14. (In Chinese)
14. Chen, S.L.; Yang, S.L.; Liu, Z. Numerical simulation of hydrodynamic performance of pentamaran in calm water base on FLUENT. *J. Jiangsu U. Sci. Technol. (Nat. Sci. Ed.)* **2012**, *26*, 541–545. (In Chinese)
15. Tarafder, M.S.; Ali, M.T.; Nizam, M.S. Numerical Prediction of Wave-making Resistance of Pentamaran in Unbounded Water using a Surface Panel Method. *Procedia Eng.* **2013**, *56*, 287–296. [[CrossRef](#)]
16. Waskito, K.T.; Jamaluddin, A. Experimental study resistances of asymmetrical pentamaran model with separation and staggered hull variation of inner side-hulls. *Int. J. Fluid Mech. Res.* **2015**, *42*, 82–94.
17. Waskito, K.T. Experimental Study of Total Hull Resistance of Pentamaran Ship Model with Varying Configuration of Outer Side Hulls. *Procedia Eng.* **2017**, *194*, 104–111.
18. Waskito, K.T.; Karim, S.; Ichsan, M. Interference resistance of pentamaran ship model with asymmetric outrigger configurations. *J. Mar. Sci. Appl.* **2017**, *16*, 42–47.
19. Yanuar; Ibadurrahman; Karim, S.; Ichsan, M. *Experimental Study of the Interference Resistance of Pentamaran Asymmetric Side-Hull Configurations*; AIP Conference Proceedings; AIP Publishing LLC: Melville, NY, USA, 2017; p. 20025.
20. Sulistyawati, W.; Yanuar; Pamitran, A.S. The influences of diversity hull shapes and outriggers arrangement in pentamaran systems. *Energy Rep.* **2020**, *6*, 595–600. [[CrossRef](#)]
21. Yanuar; Ibadurrahman; Muhammad Arif, R.; Muhamad Ryan, D.P. Resistance Characteristic of High-speed Unstaggered Pentamaran Model with Variations of Symmetric and Asymmetric Hull Configurations. *J. Mar. Sci. Appl.* **2019**, *18*, 472–481. [[CrossRef](#)]
22. Yanuar; Ibadurrahman, I.; Gunawan, A.; Wibowo, R.A. Gunawan Drag reduction of X-pentamaran ship model with asymmetric-hull outrigger configurations and hull separation. *Energy Rep.* **2020**, *6*, 784–789. [[CrossRef](#)]
23. Yanuar, G.; Utomo, A.S.A.; Luthfi, M.N.; Baezal, M.A.B.; Majid, F.R.S.; Chairunisa, Z. Numerical and experimental analysis of total hull resistance on floating catamaran pontoon for N219 seaplanes based on biomimetics design with clearance configuration. *Int. J. Technol.* **2020**, *11*, 1397–1405. [[CrossRef](#)]
24. Sulistyawati, W.; Pamitran, A.S. Warp-chine on pentamaran hydrodynamics considering to reduction in ship power energy. *Energy Procedia* **2019**, *156*, 463–468. [[CrossRef](#)]
25. Hu, P.; Cui, Y.; Zhao, C.; Li, Y.; Li, B. Numerical Investigation on the Hydrodynamic Response of Pentamaran—Resistance Analysis of Different Outrigger Inclination Angles. *J. Mar. Sci. Eng.* **2023**, *11*, 186. [[CrossRef](#)]
26. Hanjalić, K.; Popovac, M.; Hadžiabdić, M. A robust near-wall elliptic-relaxation eddy-viscosity turbulence model for CFD. *Int. J. Heat Fluid Flow* **2004**, *25*, 1047–1051. [[CrossRef](#)]
27. Song, S.; Demirel, Y.K.; Atlar, M.; Dai, S.; Day, S.; Turan, O. Validation of the CFD approach for modelling roughness effect on ship resistance. *Ocean Eng.* **2020**, *200*, 107029. [[CrossRef](#)]
28. Peri, D.; Rossetti, M.; Campana, E.F. Design optimization of ship hulls via CFD techniques. *J. Ship Res.* **2001**, *45*, 140–149. [[CrossRef](#)]
29. Zhang, Z.; Hui, L.; Zhu, S.; Feng, Z. Application of CFD in ship engineering design practice and ship hydrodynamics. *J. Hydrodyn. Ser. B* **2006**, *18*, 315–322. [[CrossRef](#)]
30. Song, S.; Demirel, Y.K.; Atlar, M. An investigation into the effect of biofouling on the ship hydrodynamic characteristics using CFD. *Ocean Eng.* **2019**, *175*, 122–137. [[CrossRef](#)]
31. Jiao, J.; Huang, S.; Soares, C.G. Numerical investigation of ship motions in cross waves using CFD. *Ocean Eng.* **2021**, *223*, 108711. [[CrossRef](#)]
32. Jasak, H.; Vukčević, V.; Gatin, I.; Lalović, I. CFD validation and grid sensitivity studies of full scale ship self propulsion. *Int. J. Nav. Arch. Ocean Eng.* **2019**, *11*, 33–43. [[CrossRef](#)]

33. Islam, H.; Ventura, M.; Soares, C.G.; Tadros, M.; Abdelwahab, H.S. Comparison between empirical and CFD based methods for ship resistance and power prediction. *Trends Mar. Technol. Eng.* **2022**, *1*, 347–357.
34. Kim, D.; Tezdogan, T. CFD-based hydrodynamic analyses of ship course keeping control and turning performance in irregular waves. *Ocean Eng.* **2022**, *248*, 110808. [[CrossRef](#)]
35. Wang, J.; Wan, D. CFD study of ship stopping maneuver by overset grid technique. *Ocean Eng.* **2020**, *197*, 106895. [[CrossRef](#)]
36. Andersson, J.; Shiri, A.A.; Bensow, R.E.; Yixing, J.; Chengsheng, W.; Gengyao, Q.; Deng, G.; Queutey, P.; Xing-Kaeding, Y.; Horn, P. Ship-scale CFD benchmark study of a pre-swirl duct on KVLCC2. *Appl. Ocean Res.* **2022**, *123*, 103134. [[CrossRef](#)]
37. Huang, S.; Jiao, J.; Soares, C.G. Uncertainty analyses on the CFD–FEA co-simulations of ship wave loads and whipping responses. *Mar. Struct.* **2022**, *82*, 103129. [[CrossRef](#)]
38. Akbarzadeh, P.; Molana, P.; Badri, M.A. Determining resistance coefficient for series 60 vessels using numerical and experimental modelling. *Ships Offshore Struct.* **2016**, *11*, 874–879. [[CrossRef](#)]
39. Yang, K.; Kim, Y. Numerical analysis of added resistance on blunt ships with different bow shapes in short waves. *J. Mar. Sci. Technol.-Jpn.* **2017**, *22*, 245–258. [[CrossRef](#)]
40. Cheng, X.; Feng, B.; Chang, H.; Liu, Z.; Zhan, C. Multi-objective optimisation of ship resistance performance based on CFD. *J. Mar. Sci. Technol.-Jpn.* **2019**, *24*, 152–165. [[CrossRef](#)]
41. Ali, M.A.; Peng, H.; Qiu, W. Resistance prediction of two fishing vessel models based on RANS solutions. *Phys. Chem. Earth Parts A/B/C* **2019**, *113*, 115–122. [[CrossRef](#)]
42. Lee, C.; Yu, J.; Choi, J.; Lee, I. Effect of bow hull forms on the resistance performance in calm water and waves for 66k DWT bulk carrier. *Int. J. Nav. Arch. Ocean Eng.* **2019**, *11*, 723–735. [[CrossRef](#)]
43. Larsson, L.; Stern, F.; Bertram, V. Benchmarking of computational fluid dynamics for ship flows: The Gothenburg 2000 workshop. *J. Ship Res.* **2003**, *47*, 63–81. [[CrossRef](#)]
44. Carrica, P.M.; Mofidi, A.; Eloot, K.; Delefortrie, G. Direct simulation and experimental study of zigzag maneuver of KCS in shallow water. *Ocean Eng.* **2016**, *112*, 117–133. [[CrossRef](#)]
45. Clark, C.G.; Lyons, D.G.; Neu, W.L. Comparison of single and overset grid techniques for CFD simulations of a surface effect ship. In Proceedings of the International Conference on Offshore Mechanics and Arctic Engineering, San Francisco, CA, USA, 8–13 June 2014; American Society of Mechanical Engineers: New York, NY, USA, 2014; pp. V2T–V8T.
46. Gu, M.; Bu, S.X.; Qiu, G.; Zeng, K.; Wu, C.; Lu, J. Validation of CFD simulation for ship roll damping using one pure car Carrier and one standard model. In Proceedings of the 15th International Ship Stability Workshop, Stockholm, Sweden, 13–15 June 2016.
47. Dong, K.; Wang, X.; Zhang, D.; Liu, L.; Feng, D. CFD research on the hydrodynamic performance of submarine sailing near the free surface with long-crested waves. *J. Mar. Sci. Eng.* **2022**, *10*, 90. [[CrossRef](#)]
48. ITTC. *Practical Guidelines for Ship CFD Applications*; Recommended Procedures and Guidelines; 2014; No. 7.5-03-02-03; Available online: <https://ittc.info/> (accessed on 27 March 2023).
49. Kim, W.J.; Van, S.H.; Kim, D.H. Measurement of flows around modern commercial ship models. *Exp. Fluids* **2001**, *31*, 567–578. [[CrossRef](#)]
50. Zhang, J.; Zhang, Y.; Guo, H. CFD numerical simulation of seakeeping performance of KCS in head waves. *Ship Eng.* **2020**, *6*, 32–40. (In Chinese)

Disclaimer/Publisher’s Note: The statements, opinions and data contained in all publications are solely those of the individual author(s) and contributor(s) and not of MDPI and/or the editor(s). MDPI and/or the editor(s) disclaim responsibility for any injury to people or property resulting from any ideas, methods, instructions or products referred to in the content.